Statistics of Randomized Plasmonic Lattice Lasers

A. Hinke Schokker and A. Femius Koenderink*

Center for Nanophotonics, FOM Institute AMOLF, Science Park 104, 1098 XG Amsterdam, The Netherlands

S *Supporting Information*

ABSTRACT: We study lasing in randomized lattices of silver particles in a dye-doped waveguide. We set out to answer a basic question, triggered by earlier observations of distributed feedback lasing in 2D periodic plasmonic particle lattices: how much order do you need to obtain lasing? We start from a diffractive 2D square lattice of silver nanoparticles with a pitch that satisfies the second-order Bragg diffraction condition at the emission wavelength of the dye. By randomly removing particles and by displacing particles we increase disorder. We observe that lasing at the second-order Bragg diffraction condition is very robust, with lasing even persisting when 99% of particles are removed. Above a certain amount of disorder new features appear in the spectrum as well as in the Fourier image that are due to random lasing. We classify Fourier space output on the basis of structure factor calculations. In addition we apply speckle intensity statistics analysis to real-space fluorescence images and introduce a new method to differentiate between spontaneous emission and lasing emission.

KEYWORDS: *plasmonic antennas, lasing, distributed feedback, random lasers*

disordered plasmon lattice lasers
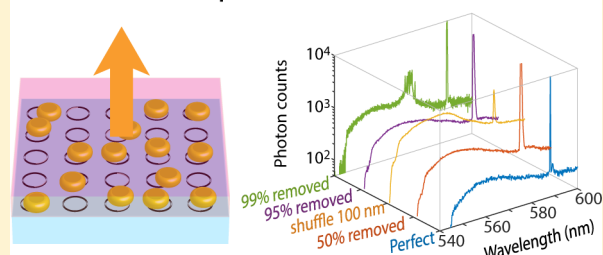
In plasmonics the interaction between light and free electrons in metal is used to obtain highly localized electromagnetic fields.[1] Over the past years plasmonics has received widespread interest because of the potential to confine light in subdiffraction-limited volumes for nanoscopy[2] and optical information processing[3] and to create huge near-field enhancement for light−matter interaction.[4] Plasmonic particles not only carry strong near fields but also scatter light much more strongly than dielectric particles of equal size. Plasmonic particles have been used as nanoscale antennas that provide up to thousand-fold fluorophore emission rate enhancement,[5−7] emission directivity,[8,9] and opportunities for surface-enhanced Raman and surface-enhanced infrared spectroscopy.[10] The properties of individual plasmon particles may be enhanced by placing particles in periodic arrays,[11] with demonstrated uses in, for example, solar cells and light-emitting diodes.[12,13] In view of the strong field enhancement effects, the interplay of gain with plasmon particles to form lasing systems is of great interest.

There are three different ways of using gain in a plasmonic system. First, propagating surface plasmons may be coupled to a gain medium so that loss compensation may be achieved.[14] Second, stimulated emission may trigger lasing into the surface plasmon or plasmon polariton mode of a single nanoparticle when sufficient feedback is provided by a plasmonic resonator.[15,16] This is known as SPASER (surface plasmon amplification by stimulated emission of radiation).[17] Third, by embedding plasmonic particle clusters in a gain medium, near-field enhancement and multiple scattering can combine to give distributed feedback lasing.[18] Several groups[19−21] showed that periodic lattices of plasmonic scatterers can yield lasing at frequencies determined by the pitch of the array through second-order Bragg diffraction, as is also the case in dielectric

distributed feedback lasers. Dielectric distributed feedback (DFB) lasers, whether as a semiconductor laser or an organic DFB laser, are widely applied devices that provide large-area and low-threshold lasing using a low index-contrast periodic grating for feedback by Bragg diffraction that is embedded in a medium that is at the same time the gain medium and a planar waveguide.[22] In a typical DFB laser, the index contrast is small, so that the waveguide dispersion is folded due to the introduced periodicity, but is otherwise hardly changed in the sense that stop gaps are narrow in spectral bandwidth. Associated with the absence of wide stop gaps is the need for DFB lasers to span large areas to build up feedback. In contrast, in the recently reported plasmon systems a characteristic large stop gap occurs in the hybridized dispersion of waveguide and plasmon lattices.[21] This results from the much larger scattering strength of metal particles. Given the unique properties of plasmonic particles in terms of their huge scattering strength compared to dielectric DFB constituents, a question that naturally arises is how robust plasmonic particle array lasers are to disorder. In between the extremes of a nominally perfectly periodic laser and a completely random laser, this question encompasses a large spectrum of "correlated disorder" cases,[23−25] in which particles are for instance progressively shuffled compared to ideal positions in a lattice or where random configurations are made by randomly removing scatterers from a perfect lattice. In this work first we treat the problem from the viewpoint of DFB lasers, in particular unraveling how much disorder a plasmon DFB laser can suffer and how disorder affects figures of merit such as threshold,
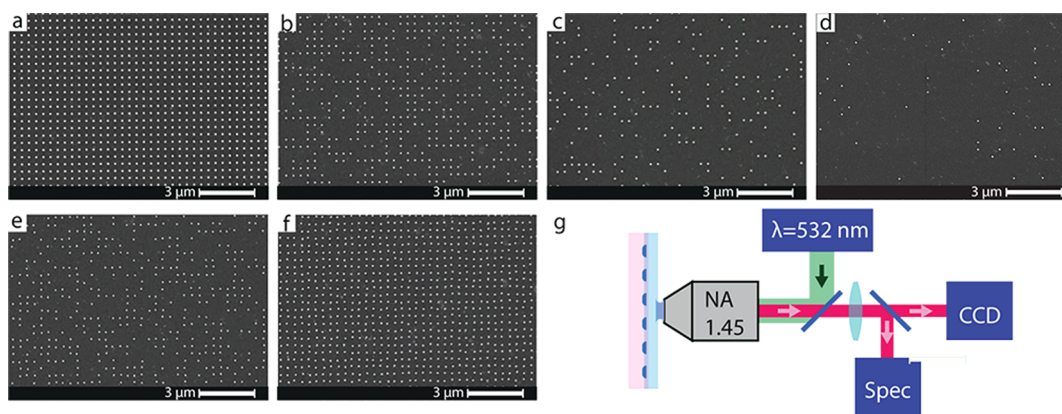
Figure 1. SEM images of randomized particle arrays (a−f) and a schematic of the setup (g). The top row (a−d) shows particle arrays in which particles have been randomly removed to leave fill factors of 100%, 50%, 20%, and 5%. Panels (e) and (f) are for fill factor of 50% and 100%, with particles randomly placed in a box of 100 nm centered on each perfect-lattice site. Scale bars in all SEM images are 3 μm. The setup diagram (g) highlights that we use a high-NA fluorescence microscope with 532 nm pulsed pump laser (0.5 ns) and a single-shot collection of spectra or alternatively CCD images in a real-space or Fourier-space imaging plane.
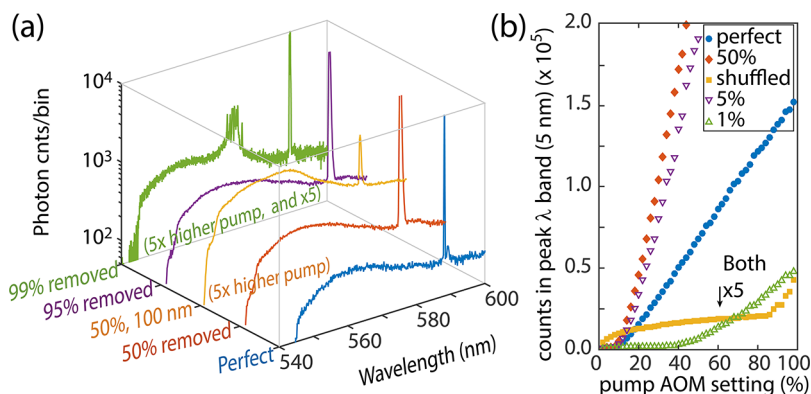

Figure 2. (a) Spectra for a perfect sample (100% fill factor, blue curve), a 50% diluted sample (red), a 50% diluted sample with 100 nm (orange), and a sample with 95% and 99% of particles removed (purple, green). Spectra are averaged over three shots and plotted on a log scale. All spectra are taken at 25 nJ pump energy, except for the two cases with a much higher threshold (50% with 100 nm shuffle and 99% removal, spectra at 240 nJ). For the case where 99% of particles were removed, the signal is furthermore multiplied by 5 to be visible on the same scale. (b) Output (lasing plus spontaneous emission) in a 5 nm band around the second-order Bragg condition as a function of input power, as controlled by the AOM (percentage of 250 nJ). Only for the very dilute sample (99%) and the sample with large shuffle do we find a much larger threshold than for the other cases. Note that the perfect sample has a smaller slope above the threshold, indicating poorer outcoupling.

outcoupling, and angular profile. In the second part of the paper we view the system from the viewpoint of disorder lasers, in particular applying speckle statistics analysis. We demonstrate that a plasmonic DFB laser is a useful platform to explore lasing in correlated disordered systems.

■ LASING IN DISORDERED SAMPLES

We fabricate silver particle arrays on glass using the electron beam lithography procedure reported in ref 21. The particles are 30 nm high silver particles of about 50 nm radius arranged (in the case of a sample without intentional disorder) in a square lattice with an interparticle separation of 380 nm. Subsequently the array is embedded in an SU8 layer (refractive index about 1.65) of 450 nm thick that simultaneously acts as single-mode transverse electric (TE) waveguide and as gain medium, through incorporation of 0.25 wt % rhodamine 6G (Rh6G). We start with a perfect periodic lattice, which we randomize using two methods. First, we knock out particles randomly from the periodic lattice. The randomness is increased by decreasing the probability of leaving a particle in the lattice, where probabilities for each site are drawn

independently. For our samples we use a probability P of 100% (periodic lattice), 50%, 20%, 10%, 5%, 2%, and 1%. As a second randomization method, we displace each particle by choosing for each a random position in a box of size l centered at their initial lattice position. We choose l to be 0, 20, 40, 60, 80, and 100 nm. Finally, we use combinations of all values of P and l. While for each lattice site the probability to keep a particle is drawn independently, we note that strong spatial correlations remain, based on the fact that particles remain situated on (or near, for $l > 0$) the ideal lattice sites. A select subset of disordered particle arrays is shown in Figure 1a−f that highlights the progression from perfect to strongly diluted samples, as well as the effect of particle shuffling. In discussing our optical measurement data throughout this article we will limit ourselves to presenting complete data for a select set of samples that highlight the salient features. These are the samples with varying fill factor (presenting $P = 100\%$, 50%, 5%, and 1%) at zero shuffle ($l = 0$) and conversely a maximum random particle displacement ($l = 100$ nm) at a fixed fill factor of $P = 50\%$. We refer to the Supporting Information for spectroscopic data on the other sample geometries.
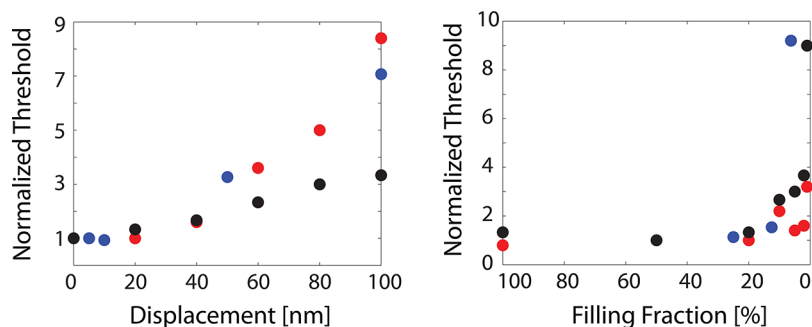
Figure 3. Threshold values normalized to the threshold for fill fraction 50% and shuffle 0 nm as a function of shuffle (a) and fill fraction (b). We report three data sets (black, blue, and red for the three series), taken on different sample substrates. While due to differences in SU8 preparation, absolute thresholds between runs are not comparable, the threshold differences show the same trends from run to run. For increasing shuffle, the lasing threshold steadily rises by at least a factor of 3. For decreasing fill fraction, we first see no threshold variation, or even a threshold reduction, until very low fill factors of <20% are reached. The spread in threshold is remarkably large for low densities.

We use an inverted fluorescence microscope (Methods section) in which the sample is excited through a high-NA objective using a pulsed 532 nm laser. A schematic of the setup is shown in Figure 1g. The schematic shows the green pump laser and the excitation and collection paths, which use the same objective. In particular we perform real-space and Fourier microscopy in an NA = 1.45 (objective Nikon Plan Apo λ 100×) fluorescence microscope, where sample excitation is realized from the glass side using 0.5 ns pulses in the range 0–250 nJ (0–10 mJ/cm²). Figure 2a shows lasing spectra for a selection of samples with progressively increasing degrees of disorder, starting from the perfect lattice (P = 100%, l = 0) in Figure 2a that lases at 590 nm, as expected from its second-order Bragg condition for the waveguide mode, set by $\lambda = n_{WG}d$, with d = 380 nm being the pitch and $n_{waveguide} \approx 1.55$ being the waveguide mode index. The mode index of n = 1.55 matches calculations[21] and can be directly read off from the Fourier images (see below). As in ref 21, the threshold is around 1 mJ/cm². When diluting the lattice, from 100% to 50% and even down to a fill factor P = 5% the lasing condition clearly remains, and in fact the threshold remains approximately constant as compared to the perfect lattice (input–output curves in Figure 2b). In absolute terms, the lattices with particles removed actually offer *more* output emission at a given pump power, for both the spontaneous emission background and the lasing peak. This indicates that disorder by moderate removal of particles aids outcoupling, but does not hamper feedback. When fixing the fill factor to P = 50% and shuffling the remaining particles by as much as 100 nm, i.e., over 25% of the pitch, lasing remains robust in the sense that a single sharp lasing peak occurs at the second-order Bragg condition of the original perfect lattice, although in this case the threshold is about 5 times higher. Finally, it is particularly surprising that even at a fill factor of 1%, when as many as 99% of the particles have been removed from the lattice, lasing persists at the Bragg condition of the perfect lattice.

The fact that the primary lasing condition remains at the second-order Bragg condition does not imply that the lasing characteristics remain unaffected by the disorder. In particular, we observe several distinct phenomena. First, as regards the lasing peak, one could expect changes in center wavelength or width. For shuffling of particles we find hardly any variation in lasing peak wavelength, while upon dilution of the lattices, the peak laser wavelength varies by around 2 nm. The width of the lasing peak, as determined from the first spectrum above the threshold, is at the spectrometer resolution for all cases (see

Supporting Information for quantification for all filling factors and shuffles). Second, the lasing threshold (plotted in Figure 3) gradually increases by up to a factor of 3 as we increase the random displacement l from 0 nm to 100 nm, at a fixed lattice fill factor of 50%. In Figure 3 we plot thresholds for several independent experiment runs on different samples with nominally identical parameters, where in each run we normalized thresholds to that of the sample with a 50% fill factor and no shuffle (arbitrarily chosen as our reference sample). This normalization procedure reduces variations between samples that are due to differences in polymer thickness or doping that might occur between different sample fabrication runs. That the thresholds are immune to displacement of particles up to between 20 and 40 nm is common among all samples, as is the fact that the threshold rises for higher displacement. For the case of decreasing fill factor P (at no shuffle), the threshold behavior is less intuitive. Thresholds for the lattices with a fill factor of 100% down to 20% are all comparable. We attribute this remarkable result to the fact that the particles on one hand are required to provide feedback by scattering, yet on the other hand constitute a loss channel through absorption. Since the particles are very strongly scattering compared to those that suffice to achieve lasing in DFB lasers, it is reasonable that removing 50% to 80% of them leaves sufficient feedback by scattering and in fact may even reduce threshold by reducing absorption. We find a marked increase in threshold only for fill factors below 20%, from which point on we find not only an increase but also a wide spread in threshold. We attribute the much increased spread in lasing thresholds observed for very low fill factors to a third change in the lasing behavior that is evident from examining the spectra. The spectra themselves at very low fill factor show the appearance of extra emission peaks distinct from the λ = 590 nm Bragg condition at markedly blue-shifted wavelengths that are much closer to the main emission band of Rh6G (Figure 2a, green spectrum). We hypothesize that at large fill factors, above 20%, the randomized lasers essentially remain DFB lasers that function near the original diffraction condition, but with thresholds that increase with increasing particle shuffle. At very low fill factors qualitatively different behavior emerges, where 2D DFB lasing competes with behavior reminiscent of random lasing.[26,27]

To rationalize the fact that lasing persists even at very large levels of disorder, especially in terms of lattice dilution, we consider the structure factors of the various (dis)ordered lattices. The structure factor is defined as the Fourier transform

of the lattice of particle center coordinates. Figure 4 shows structure factors for the perfect, periodic, lattice as well as a
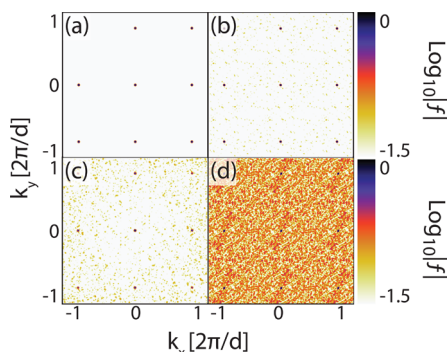

Figure 4. Fourier transform of a lattice with fill fraction 100% and shuffle 0 (a), fill fraction 50% and shuffle 0 nm (b), fill fraction 50% and shuffle 100 nm (c), and fill fraction 5% and shuffle 0 nm (d). The color scale is normalized to the FT maximum.

50% diluted lattice, a 50% diluted lattice with maximum shuffle (100 nm), and a lattice of fill factor 5%. Evidently, when diluting the lattice by 50%, even at maximum particle displacement, the structure factor still shows clear Fourier peaks at the ideal-lattice reciprocal lattice vectors. At maximum shuffle, the Fourier peaks decrease moderately in intensity, and a background appears of speckle that is especially evident at larger k. In contrast, at very low fill factor the Fourier peaks are only just evident above the speckled background that is typical for a completely random system. To conclude, by "merely" reducing the lattice fill factor to 50% or 20%, very strong spatial correlations remain, explaining why the original second-order Bragg condition is clearly available for lasing. Likewise, randomizing particle locations by $l = 100$ nm does not strongly reduce the spatial correlations. Only in the case of strongly reducing the lattice fill factor do spatial correlations become faint. Besides an analysis of the structure factor, which accounts for only the particle ordering, lasing naturally also depends on

the gain length and particle scattering strength. The gain length of the Rh6G (3×10^{-20} m^2 cross section)-doped waveguide layer is estimated as ∼4 μm, or 10 unit cell spacings, at the maximum pump intensity. Lasing is thus aided by the fact that the 2D planar waveguide geometry strongly favors amplification of in-plane scattered light, with a short gain length comparable to the interparticle distance. As regards scattering strength, in ref 21 it was established for the "perfect" periodic lattice (no intentional disorder) that the Ag particles are sufficiently strongly scattering to open a clear, 3% wide stop gap at the second-order Bragg condition. This is a key number, since the inverse of the relative stop gap width is a direct measure for the Bragg length, i.e., the number of unit cells required for Bragg reflection.[28] In dielectric DFB structures lasing is achieved under conditions where the scattering strength per unit cell is very small, meaning that not just 30 lattice spacings (or scatterers) provide sufficient feedback for lasing, but on the order of 10^3 are needed.[29] Indeed, as we reported in ref 21, the exact same lasing geometry but with Ag replaced by the highest index possible for a dielectric (TiO$_2$), we could not even obtain lasing given the pump area of about 150 lattice spacings across. With particles twice the volume, we barely obtained sufficient feedback for lasing. This rationalizes that for the plasmonic particles, even at a strong reduction of the scattering strength per unit cell, there is sufficient distributed feedback for lasing, whether that reduction is obtained by shrinking particles or removing them altogether. An interesting question is if upon diluting the lattice, scattering measurements in the absence of gain can be used to resolve the width of the bands and the width of the stop gap. In practice, however, we note that such experiments are hardly feasible. Figure 5, further discussed below, shows that the passive-system features that are due to Bragg diffraction vanish in amplitude upon dilution, even though upon amplification they stand out. Given the particle cross section of about 0.07 μm^2, expected transmission features have only a few percent amplitude at dilutions to 20% or less. We note that a *full* theory of lasing in these systems is beyond the scope of this paper. In fact, even for the perfect periodic case, there is currently no theory that covers simultaneously the
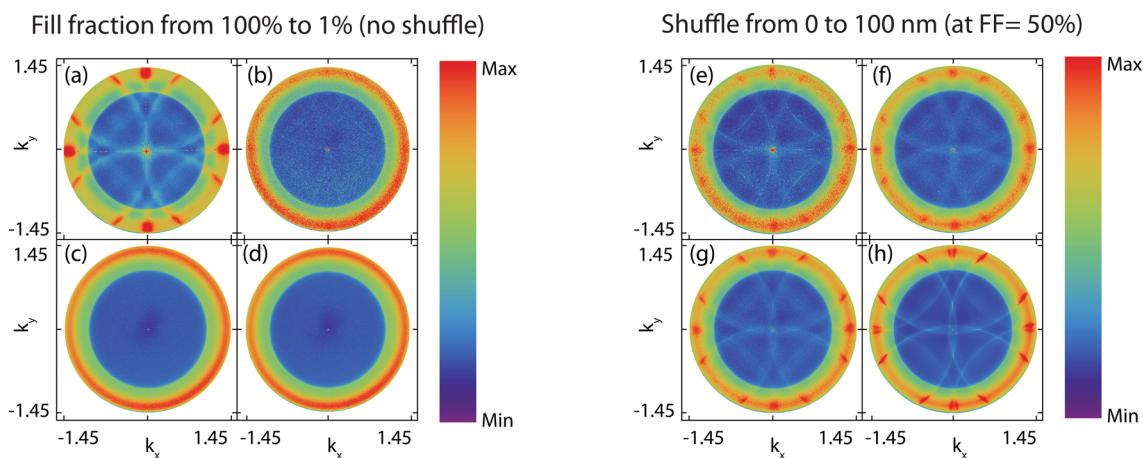

Figure 5. Back focal plane images taken at a pump power just a few percent above threshold for plasmon lattice lasers that are randomized by diluting from 100% to 20%, 5%, and 1% fill factor (a−d) and by shuffling (e−h, fixed 50% fill factor) by 0, 40, 60, and 100 nm. The color axes in all cases are chosen to obtain a dynamic range of around 5, spanning mean × [0.35 1.8] around the mean image intensity. Specifically, for the background-subtracted images, the ranges are [min, max] = [154, 700], [199, 1050,], [212, 1144], [264, 1503] for (a)−(d) and [174, 946], [204, 1095], [282, 1525], [402, 2257] for (e)−(h), where numbers correspond to background-subtraced CCD counts (about 3 photoelectrons per count) in single-shot images. The horizontal and vertical axes are in units of $k_0 = \omega/c$, i.e., in units of numerical aperture. In all cases the lasing output is visible as an intense spike at $\mathbf{k}_\parallel = 0$, as well as to varying degrees as speckle.

plasmonic lattice dispersion, gain, and the emergence of lasing from noise.[30]

FOURIER SPACE ANALYSIS

The structure factor analysis directly motivates a study of Fourier images to further understand the distinct lasing characteristics at various types of disorder. Fourier images or "back focal plane" images for the perfectly ordered case ($P = 100\%$ and $l = 0$) were discussed in depth in ref 21. In brief, they present the following appearance (Figure 5a) for below-threshold emission. They appear as bright disks on the CCD where the center corresponds to the optical axis, and the distance from the center outward is proportional to $|k_\parallel|/k_0 = n \sin\theta$ (θ is the emission angle into glass). Thus, the outer edge of the disk corresponds to the NA of the objective, which is equal to 1.45. The inner circle corresponds to an NA of 1 (i.e., $|k_\parallel| = \omega/c$). It is due to the fact that below threshold most emission exits the dye layer at an angle just above the critical angle for the air/glass interface, i.e., at an NA greater than 1, which is a well-known property of the emission pattern of dipole emitters held just above a glass interface.[31] In addition to these sharp concentric circles, eight broad, diffuse, circles appear that are not centered at the origin, but rather are centered at the reciprocal lattice vectors $\mathbf{k}_\parallel = 2\pi/d(m, n)$ (with d being the particle pitch and m, n integers) and have radius $k_0 \times n_{\text{waveguide}}$. Here $n_{\text{waveguide}}$ is the effective refractive index of the waveguide mode, in between the index of glass and the refractive index of the SU8 layer ($n_{\text{SU8}} = 1.65$). Thus, the waveguide mode index $n_{\text{waveguide}} \approx 1.55$ can be directly read off from the radius of curvature of the observed bands. In solid-state physics terms, these images represent repeated-zone-scheme isofrequency surfaces of the nearly free waveguide dispersion relation, blurred by the spectral bandwidth of the dye. Note that these circles appear to touch at $k_\parallel = 0$, indicating that the pitch is such that the second-order Bragg condition is met for waveguide modes at wavelengths close to the emission band of Rh6G. The below-threshold Bragg diffracted waveguide modes, i.e., the circles, are broad because the Fourier images are panchromatic, and different wavelengths yield circles centered at somewhat different origins. Strictly, the circles touch in the center for just one emission wavelength, which is equal to the lasing wavelength (590 nm, see Figure 2a). When the system reaches the lasing threshold, a central lasing spot emerges at $k_\parallel = 0$ (center of the image), as can be seen in all Fourier images in Figure 5.

Figure 5 shows back focal plane images for disordered samples at pump powers just a few percent above the lasing threshold, so that, besides the emission at $k_\parallel$ from the lasing mode, the wave vector structure for spontaneous emission can still be made out, as can be seen from the circles in Figure 5a. Figure 5b,c,d show Fourier images for samples in which we reduced the fill factor of the lattice to 20%, 5%, and 1%, respectively. Going from 100% to 20% fill factor, two facts stand out. First, the back aperture is now filled with distinct speckle. The emergence of speckle directly points at the spatial and temporal coherence of the lasing mode. We attribute the emergence of speckle to the fact that lasing that in the 100% case only couples out as a $k_\parallel = 0$ beam can randomly scatter at the introduced disorder, thereby distributing intensity over the back aperture. The second remarkable observation is that, compared to the ordered sample, the repeated circles are only faintly observable. At even lower fill factor the repeated circles completely disappear. This stands in good agreement with the

fact that for randomly removed particles the reciprocal lattice in the structure factor rapidly loses contrast. For the strongest dilution the speckle itself decreases in visbility, owing to the fact that the associated increase in threshold causes an increase in broad background emission as a consequence of the increased pump intensity.

Fourier images at a fixed, high fill factor of 50%, but increasing degree of disorder introduced by shuffling present a very different evolution of Fourier images. Figure 5e−h show Fourier images for pump energies just above the lasing threshold for a 50% fill factor at $l = 0$, $l = 40$, $l = 60$, and $l = 100$. At all degrees of shuffle, even as large as 100 nm, the repeated-zone-scheme dispersion relation remains clearly evident as repeated circles. In most instances we in fact see two sets of repeated-zone-scheme dispersion. Our interpretation is the following. The "inner" set of circles, which is narrow in width and speckled and that touches at $k_\parallel = 0$, corresponds to lasing emission. The fact that scattering of the laser light does not lead to a homogeneous distribution of speckle over the back aperture as in the case of strongly diluted lattices shows that the high-fill-factor lattices with displaced particles are disordered yet still strongly correlated. The width of the circles reflects the spectrally narrow lasing line, while the speckled nature shows spatial coherence of the lasing mode. The "outer" set of circles is broader and diffuse. They correspond to incoherent Rh6G emission at shorter wavelength, i.e., at the Rh6G spontaneous emission maximum. These circles become more apparent at higher disorder, as a consequence of the much higher threshold pump intensity at which the image needs to be acquired. The experimental observation that whereas the dilute lattices hardly show evidence for the underlying repeated-zone-scheme dispersion relation, while dense lattices clearly do, is easily understood from considering the structure factor of the underlying lattice (Figure 4), in which the reciprocal lattice still clearly stands out.

REAL-SPACE SPECKLE STATISTICS

So far we have examined the lasers as perturbed versions of the ideal, periodic, plasmonic DFB laser, asking how performance "suffers" upon introducing disorder. From a very different perspective, our plasmonic lasing platform is of large current interest in another field of research, i.e., lasing in random systems and in systems with correlated disorder.[23−25] In that field, rather than studying Fourier images for residual diffraction conditions, one rather focuses on the statistical properties of speckle. Above the lasing threshold, one expects the emitted light to be spatially coherent across an extended area of the structure. Interference between coherent scattered waves in a random medium will generate a grainy pattern that is known as speckle,[32] for which the random scattering community has developed quantitative analysis tools. These analysis tools map intensity distributions, as well as spatial/angular correlations. In the context of random lasers, for instance, intensity statistics of speckle have been studied as a function of pumping strength.[26,27] While for perfectly uncorrelated disorder, speckle statistics follow robust laws, deviations from these laws are of even larger interest, as they can for instance point at localization effects, are sensitive probes of otherwise poorly quantifiable scattering correlations, and can be used to quantify rare, but dramatic events in correlated disorder systems.[33]

Example real-space images below and above the threshold for the laser with fill factor $P = 50\%$ and no further shuffling $l = 0$ nm are shown in Figure 6a and b. Below the threshold, the
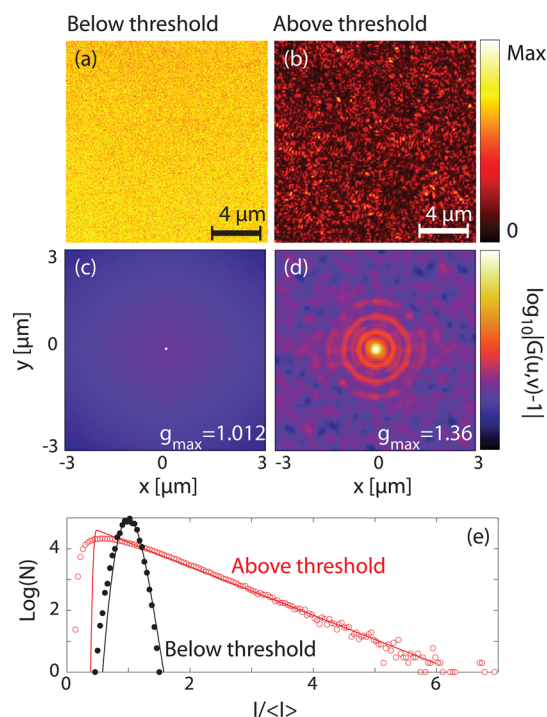
Figure 6. Real-space fluorescence images below (a) and above (b) threshold for an array with fill factor 50% and no particle shuffling. The pump powers are at about 20 at 250 nJ for panels (a) and (b), and the color scales span to 180 and 10 000 counts, respectively. Panels (c) and (d) show the respective autocorrelations, using a color scale that is linear in $\lVert\log_{10}G(u, v) - 1\rVert$, covering the range for $G(u, v)$ from [1.003, 1.012] in (c) to [1.001, 1.36] in (d). The intensity statistics for below threshold data are Poissonian (black dots, distribution with no adjustable parameter), while the above-threshold speckle shows a much longer tail (red dots). Overplotted is the expected statistics for the sum of incoherent Poisson-distributed emission (contributing $\alpha = 60\%$ of the intensity and speckle with pure Rayleigh statistics). The intensity statistics are plotted as a function of $I/\langle I\rangle$ using as vertical scale the log of the number of occurrences. The statistics use $\sum N = 6.1 \times 10^4$ image pixels.

emission is essentially constant over the field of view (about 20 μm across, set by the pump spot size) with a small pixel-to-pixel variation that is consistent with Poisson noise. This behavior is commensurate with expected behavior for fluorescence. That the particle lattice, which in principle is resolvable with white light illumination, does not stand out is likely due to the fact that the waveguide height (450 nm) far exceeds the particle height, meaning that most fluorophores do not enjoy a strong local field enhancement. Above threshold the real-space fluorescence image is entirely different, with signal variations from position to position comparable in magnitude to the mean intensity itself, as expected for a speckle pattern.

To investigate spatial correlations, we show the normalized autocorrelation in Figure 6c and d. The normalized autocorrelation is given by

$$G(u, v) = \frac{\iint I(x, y)\, I(x - u, y - v)\, \mathrm{d}x\, \mathrm{d}y}{\left(\iint I(x, y)\, \mathrm{d}x\, \mathrm{d}y\right)^2} \tag{1}$$

In this definition complete uncorrelated images yield $G(u, v) = 1$, whereas any spatial correlation will result in $G(u, v) \neq 1$.

Below threshold, the real-space images yield a normalized autocorrelation that is flat and 1, except for a single-pixel-wide

peak at $(0, 0)$. For a fluorescence emission image where each pixel follows an independently drawn Poisson statistics, one indeed expects $G = 1$, except at $(u, v) = (0, 0)$, where a small excess correlation is expected for Poisson noise, of $G(0) = 1 + 1/\langle I\rangle$, with $\langle I\rangle$ being the mean intensity. Thus, the autocorrelation of our below-threshold data is in excellent accord with uncorrelated fluorescence emission from a homogeneous dye film. Above threshold two features change. First, the autocorrelation shows a much higher maximum value of around 1.36 at $(u, v) = (0, 0)$, well above $1 + 1/\langle I\rangle$. Second, also away from $(u, v) = (0, 0)$ there is a clear correlation, with distinct circles appearing around the central peak. For a speckle pattern that results from uncorrelated disorder through superposition of plane waves of random phase and amplitude, one expects the autocorrelation to exhibit a sinc-type oscillatory behavior with a typical width at half-maximum equal to the diffraction limit and a maximum of 2, at least for purely random, but fully coherent, speckle.[32,34] Our data are in good qualitative agreement with this expectation, barring two features. First, we note that the square nature of the underlying lattice is faintly visible in the autocorrelation, directly indicating the correlated nature of the disorder.[35] Second, the autocorrelation contrast of 2 is not reached. We attribute this to the fact that, above threshold, images are a summation of incoherent and uncorrelated spontaneous emission that is broadband, plus the speckle pattern resulting from the spectrally narrowband lasing mode (see Figure 2). Indeed, with increasing pump power above threshold we find increasing autocorrelation contrast (see below). Clearly, the crossing of the laser threshold is dramatically present in the real-space autocorrelation images as a transition from completely uncorrelated to showing a distinct spatial autocorrelation commensurate with a speckle pattern.

Beyond the spatial autocorrelation function, a second tool to analyze speckle is intensity statistics.[26,27,32,34] When speckle is generated as a sum of waves with independently varying amplitudes and randomly distributed phases (uniformly distributed over 2π), the intensity is expected to be distributed according to the so-called Rayleigh distribution,[26,27,32,34] given by

$$P_{\mathrm{Rayleigh}}(I; \langle I\rangle) = \frac{1}{\langle I\rangle} e^{-I/\langle I\rangle} \tag{2}$$

where $\langle I\rangle$ represents the mean intensity. Speckle generally satisfies the Rayleigh distribution, unless it results from strongly correlated scattering events and assuming that corrections due to polarization effects can be disregarded. Importantly, the exponential form of the Rayleigh distribution implies that a histogram of $P(I/\langle I\rangle)$ versus $I/\langle I\rangle$ on a semilogarithmic scale simply yields a line of slope -1, independent of the sample, provided that the scattering events randomize phase. Below the lasing threshold, we would expect markedly different intensity statistics, since when fluorophores emit photons incoherently, the intensity will simply follow a Poissonian intensity distribution:

$$P_{\mathrm{Poisson}}(I; \langle I\rangle) = \frac{\langle I\rangle^I}{I!} e^{-\langle I\rangle} \tag{3}$$

Figure 6e shows intensity histograms for the below and above-threshold image of Figure 6a,b. The below-threshold intensity histogram generated from Figure 6a is sharply peaked around the mean per-pixel count. It is excellently described by the

Poisson distribution, without any adjustable parameter. In stark contrast, the intensity histogram for the above-threshold data set of Figure 6b is not sharply peaked but shows a long, linear tail that is indicative of an exponential dependence as expected for Rayleigh statistics. However, the exponent is not equal to −1. As an explanation, we note that just above threshold one expects the collected emission to be the sum of incoherent spontaneous emission plus the speckle pattern generated by the lasing mode, with a ratio between the two that changes as one further exceeds threshold. To benchmark this assertion, we compare the data to the joint probability distribution for the sum of an independently drawn Poisson process and Rayleigh statistics:

$$P_{joint}(I; \langle I \rangle, \alpha) = \int_0^I P_{Poisson}(I_1; \alpha \langle I \rangle) P_{Rayleigh}(I - I_1; (1 - \alpha)\langle I \rangle) \, dI_1$$

$$\approx e^{-I/[\langle I \rangle (1 - \alpha)]} \frac{e^{\alpha/(1 - \alpha)}}{2(1 - \alpha)} \left\{ \mathrm{erf}\left[\sqrt{\frac{\alpha \langle I \rangle}{2}} \right] - \mathrm{erf}\left[\sqrt{\frac{\alpha \langle I \rangle}{2}} (1 - I/\sqrt{\alpha \langle I \rangle}) \right] \right\}$$

Here the only free parameter is the ratio $0 \leq \alpha \leq 1$ defined as the fraction of signal contributed by the Poisson background. The approximate expression results from applying a Gaussian approximation to the Poisson distribution and requires $\alpha \langle I \rangle \gtrsim 50$ counts and reasonably large argument I (rule of thumb $I > \alpha \langle I \rangle$). It shows that the large intensity tail is again exponential, but with exponent steepened by a factor $(1 - \alpha)$. Therefore, to compare the joint probability function, we fit to the slope of the high-intensity tail. Indeed, now we obtain a good match to the data, again containing no vertical scaling whatsoever. For the example data set, in Figure 6d, the fit indicates that $\alpha = 0.6$, meaning that 60% of the total intensity is contributed by incoherent emission and 40% by lasing. As the pump power increases from 25 nJ to 250 nJ, the value of α decreases from 0.96 to 0.6.

To summarize our results from analyzing real-space images for a particular randomized laser, the above-threshold emission shows an autocorrelation commensurate with that expected for random speckle, with a contrast at $(0, 0)$ that rises from 1 (incoherent background) yet remains well below 2 (expected for just speckle). We attribute this to the fact that emission is a sum of incoherent (fractional contribution α) and coherent emission. This same hypothesis also is consistent with the intensity statistics, from which we fit α. We now proceed to show that the normalized autocorrelation contrast at $(0, 0)$ and the intensity ratio α are directly related. One can easily derive the expected autocorrelation for a 2D data set that is the sum of coherent and incoherent radiation in terms of the autocorrelations of each constituent. Supposing once again a mean intensity $\langle I \rangle$ of which a fraction α is contributed by uncorrelated Poisson distributed emission and a fraction $1 - \alpha$ from pure speckle (autocorrelation 2), one expects

$$g_{max} = 1 + (1 - \alpha)^2 + \frac{\alpha}{\langle I \rangle} \tag{4}$$

where g_{max} is the value of the normalized autocorrelation at $(u, v) = 0$. Typically one can neglect the $\alpha/\langle I \rangle$ term, and the normalized maximum autocorrelation relates to $1 - \alpha$ as $g_{max} = 1 + (1 - \alpha)^2$. Figure 7 shows g_{max} as a function of α for all values of P and l and for all 50 pump powers between 0 and 250 nJ. Each data set traces out the following dependence as a function of pump power. Below threshold, we find g_{max} starting at around 1.05 ($g_{max} = 1 + 1/\langle I \rangle$, with 20 counts per pixel in our lowest pump power images) and closing in on $g_{max} = 1$ as pump

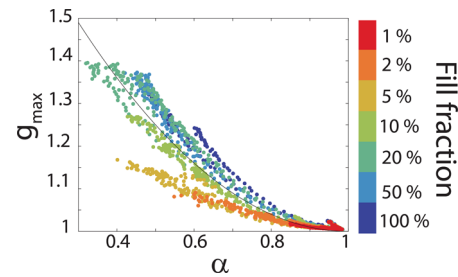**Figure 7.** Plot of g_{max}, i.e., the maximum value of the real-space autocorrelation, versus α, i.e., the ratio of the incoherent Poisson-distributed emission to the total system output, as fitted from the slope of the tail of the intensity statistics. This plot assembles pump-power-dependent traces for all values of P and l, where different fill fractions are indicated by the color coding (no coding used for shuffle). The black curve represents the expected universal behavior in eq 4. For each sample, as a function of pump power the curve starts near (g_{max}, α) = (1.05, 0.95) and α = 0.95 for the lowest pump power, approaching (1.0, 1.0) as the pump power is increased, until the threshold is exceeded. From that point on, data rapidly trace upward in g_{max} along the parabola.

power is increased toward threshold. At this stage, α is essentially 1 throughout. As soon as the threshold is crossed, the data trace out the parabolic dependence $g_{max} = 1 + (1 - \alpha)^2$, meaning that simultaneously α decreases well below 1 and g_{max} increases well above 1.

To first order, we indeed find that all data sets cluster around the predicted parabola of eq 4 (black curve). Closer inspection of Figure 7 surprisingly shows systematic deviations from this picture. In particular, the randomized plasmonic lattices with high fill factor show spatial correlations (g_{max} above the parabola) that exceed the expectation derived from intensity statistics, while conversely for the randomized plasmonic lattices with low fill factors, below 5%, the data remain significantly below the parabola. The latter indicates that the intensity statistics are more wildly fluctuating (α further from 1) than the spatial autocorrelation predicts. We propose that the fact that there is a systematic deviation from the expectations derived for purely uncorrelated disorder is an important starting point for future investigations: it shows that 2D random plasmon arrays are an exciting platform to study lasing in correlated disorder systems. For instance, for the very dilute systems, we hypothesize that we enter the regime where our field of view can contain several uncoupled and spatially separated random lasing modes simultaneously. To support this notion, in Figure 8 real-space images and spectra for this particular subset of dilute samples are shown. The above-threshold spectrum for fill fraction 1% and shuffle 0 nm is significantly different from that in dense arrays, with the appearance of multiple narrow, apparently randomly located peaks in a band around λ = 570 nm. The above-threshold real-space image exhibits clusters of speckle on a diffuse background, instead of uniform speckle. This supports the notion that this sample supports isolated lasing at spatially separated clusters of particles. We envision that similar analysis can be applied to a plethora of other designer disordered structures, random lasers, and Anderson localization systems, to resolve what are the lowest loss modes.

■ OUTLOOK

To conclude, in this paper we have shown that plasmonic DFB lasers are remarkably robust to the introduction of positional
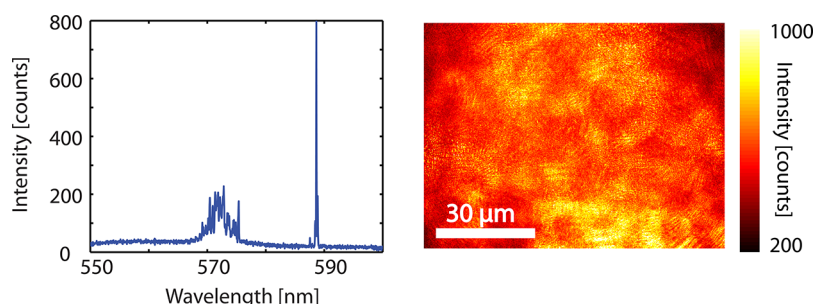
Figure 8. Spectrum and real-space image above threshold for a plasmon array laser with a fill fraction of just 1% and shuffle 100 nm. The spectrum clearly shows lasing at the second-order Bragg condition of the perfect lattice, near 590 nm. In addition, the spectrum shows many random sharp peaks, clustered around a wavelength of 570 nm. This band coincides with the gain maximum. These peaks do not occur for dense arrays and are attributed to random lasing (out)competing DFB lasing. The real-space image shows another distinct feature of diluted systems. Instead of exhibiting a uniform speckle pattern, clusters of speckle appear, on top of a diffuse background.

disorder, as well as to random removal of particles from the lattice. In fact, even upon removal of as many as 99% of the particles from a periodic lattice, a lasing peak centered on a original Bragg peak of the lattice remains. We attribute the remarkable resilience of lasing in this system to two characteristics of our geometry. On one hand, the basic geometry of a 2D waveguide with high gain favors lasing strongly, owing to the fact that the confinement along one direction creates a strong tendency for in-plane amplification of spontaneous emission (ASE).[22] We estimate a gain length of just 10 to 15 lattice periods. The second unique characteristic is that plasmonic particles are exceptionally strongly scattering. As we found in our analysis of the purely periodic lattice, the plasmon particles scatter over 20 times more strongly than dielectric particles of comparable size. As a size estimate, the inverse of the relative width of the band structure stop gap (3%) of the periodic system provides as an estimate that Bragg diffraction requires a distance of just 15 μm (30 unit cells). Hence it is understandable that "moderate dilutions", meaning removal of 50% to 80% of the particles, leaves sufficient feedback by scattering, yet without any penalty in threshold. One could argue that removing particles may even *lower* the threshold owing to the fact that it reduces the likelihood of ohmic damping. An interesting future experiment is to understand precisely what the optimum filling fraction for the lowest lasing threshold is, with respect to particle scattering and absorption cross sections. In addition, an exciting outlook of this work is that, besides the obvious interest for applications of disorder-immune lasing behavior, the geometry of a planar organic waveguiding system with metal particle lattices or oligomers is very amenable to studies of lasing in correlated disordered systems.[24,25] The plasmon particle arrays are very easy to make by lithography and are embedded in an easily fabricated gain medium that allows for simple room-temperature experiments. Thus, they could enable studies of lasing in random 2D systems and systems with correlated disorder that are now performed using perforated III−V semiconductor membranes.[25] Using the techniques of organic electronics, one could furthermore envision scenarios in which electrically driven operation is possible.

■ METHODS

Data are collected in an NA = 1.45 (objective Nikon Plan Apo λ 100×) fluorescence microscope, where sample excitation is realized from the glass side using 0.5 ns pulses in the range 0−250 nJ (0−10 mJ/cm^2). To measure input−output curves, we measure emission spectra (Shamrock f/4 30 cm spectrometer, with 300 lines/mm grating, and an Andor iVac Si CCD camera) at increasing pump power, where the input laser power is modulated using an acousto-optic modulator (AOM). Fluorescence is detected through the same objective, and after passing through a dichroic mirror fluorescence is sent to the spectrometer or to a CCD camera for real-space and Fourier imaging. In front of the tube lens of the CCD (Andor Clara) there is an extra lens on a flip-mount to switch between real-space imaging and Fourier imaging, by imaging of the back focal plane of the objective. We perform single-shot measurements to prevent bleaching of the dye from influencing our measurements. For all particle arrays we measure for a sequence of 50 pump powers in succession Fourier images, spectra, and real-space images. We refer to ref 21 for further technical details of the detection geometry.

■ ASSOCIATED CONTENT

ⓢ Supporting Information

The Supporting Information is available free of charge on the ACS Publications website at DOI: 10.1021/acsphotonics.5b00226.

> Calculations of scattering cross sections for silver particles, as well as spectroscopy data for all fill factors (at zero shuffle) and for all shuffles from 0 to 100 nm at fixed 50% fill factor (PDF)

■ AUTHOR INFORMATION

Corresponding Author
*E-mail: f.koenderink@amolf.nl.

Notes
The authors declare no competing financial interest.

■ ACKNOWLEDGMENTS

■ REFERENCES

(1) Maier, S. A. *Plasmonics: Fundamentals and Applications*; Springer: Berlin, 2007.

(2) Taminiau, T. H.; Moerland, R. J.; Segerink, F. B.; Kuipers, L.; van Hulst, N. F. $\lambda/4$ Resonance of an Optical Monopole Antenna Probed by Single Molecule Fluorescence. *Nano Lett.* **2007**, *7*, 28–33.

(3) Han, Z.; Bozhevolnyi, S. I. Radiation guiding with surface plasmon polaritons. *Rep. Prog. Phys.* **2013**, *76*, 016402.

(4) Agio, M.; Alù, A. *Optical Antennas*; Cambridge University Press, 2013.

(5) Kinkhabwala, A.; Yu, Z.; Fan, S.; Avlasevich, Y.; Muellen, K.; Moerner, W. E. Large single-molecule fluorescence enhancements produced by a bowtie nanoantenna. *Nat. Photonics* **2009**, *3*, 654–657.

(6) Punj, D.; Mivelle, M.; Moparthi, S. B.; van Zanten, T. S.; Rigneault, H.; van Hulst, N. F.; García-Parajo, M. F.; Wenger, J. A plasmonic 'antenna-in-box' platform for enhanced single-molecule analysis at micromolar concentrations. *Nat. Nanotechnol.* **2013**, *8*, 512–516.

(7) Akselrod, G. M.; Argyropoulos, C.; Hoang, T. B.; Ciraci, C.; Fang, C.; Huang, J.; Smith, D. R.; Mikkelsen, M. H. Probing the mechanisms of large Purcell enhancement in plasmonic nanoantennas. *Nat. Photonics* **2014**, *8*, 835–840.

(8) Belacel, C.; Habert, B.; Bigourdan, F.; Marquier, F.; Hugonin, J.-P.; Michaelis de Vasconcellos, S.; Lafosse, X.; Coolen, L.; Schwob, C.; Javaux, C.; Dubertret, B.; Greffet, J.-J.; Senellart, P.; Maitre, A. Controlling Spontaneous Emission with Plasmonic Optical Patch Antennas. *Nano Lett.* **2013**, *13*, 1516–1521.

(9) Langguth, L.; Punj, D.; Wenger, J.; Koenderink, A. F. Plasmonic Band Structure Controls Single-Molecule Fluorescence. *ACS Nano* **2013**, *7*, 8840–8848.

(10) Le, F.; Brandl, D. W.; Urzhumov, Y. A.; Wang, H.; Kundu, J.; Halas, N. J.; Aizpurua, J.; Nordlander, P. Metallic nanoparticle arrays: A common substrate for both surface-enhanced Raman scattering and surface-enhanced infrared absorption. *ACS Nano* **2008**, *2*, 707–718.

(11) Zhao, L.; Kelly, K. L.; Schatz, G. C. The Extinction Spectra of Silver Nanoparticle Arrays: Influence of Array Structure on Plasmon Resonance Wavelength and Width. *J. Phys. Chem. B* **2003**, *107*, 7343–7350.

(12) Mokkapati, S.; Catchpole, K. R. Nanophotonic light trapping in solar cells. *J. Appl. Phys.* **2012**, *112*, 101101.

(13) Lozano, G.; Louwers, D. J.; Rodriguez, S. R. K.; Murai, S.; Jansen, O. T. A.; Verschuuren, M. A.; Rivas, J. G. Plasmonics for solid-state lighting: enhanced excitation and directional emission of highly efficient light sources. *Light: Sci. Appl.* **2013**, *2*, e66.

(14) Berini, P.; De Leon, I. Surface plasmon-polariton amplifiers and lasers. *Nat. Photonics* **2011**, *6*, 16–24.

(15) Oulton, R. F.; Sorger, V. J.; Zentgraf, T.; Ma, R.-M.; Gladden, C.; Dai, L.; Bartal, G.; Zhang, X. Plasmon lasers at deep subwavelength scale. *Nature* **2009**, *461*, 629–632.

(16) Ma, R.-M.; Oulton, R. F.; Sorger, V. J.; Bartal, G.; Zhang, X. Room-temperature sub-diffraction-limited plasmon laser by total internal reflection. *Nat. Mater.* **2011**, *10*, 110–113.

(17) Bergman, D. J.; Stockman, M. I. Surface plasmon amplification by stimulated emission of radiation: Quantum generation of coherent surface plasmons in nanosystems. *Phys. Rev. Lett.* **2003**, *90*, 027402.

(18) Stehr, J.; Crewett, J.; Schindler, F.; Sperling, R.; von Plessen, G.; Lemmer, U.; Lupton, J. M.; Klar, T. A.; Feldmann, J.; Holleitner, A. W.; Forster, M.; Scherf, U. A low threshold polymer laser based on metallic nanoparticle gratings. *Adv. Mater.* **2003**, *15*, 1726–1729.

(19) Suh, J. Y.; Kim, C. H.; Zhou, W.; Huntington, M. D.; Co, D. T.; Wasielewski, M. R.; Odom, T. W. Plasmonic Bowtie Nanolaser Arrays. *Nano Lett.* **2012**, *12*, 5769–5774.

(20) Zhou, W.; Dridi, M.; Suh, J. Y.; Kim, C. H.; Co, D. T.; Wasielewski, M. R.; Schatz, G. C.; Odom, T. W. Lasing action in strongly coupled plasmonic nanocavity arrays. *Nat. Nanotechnol.* **2013**, *8*, 506–511.

(21) Schokker, A. H.; Koenderink, A. F. Lasing at the band edges of plasmonic lattices. *Phys. Rev. B: Condens. Matter Mater. Phys.* **2014**, *90*, 155452.

(22) Samuel, I. D. W.; Turnbull, G. A. Organic semiconductor lasers. *Chem. Rev.* **2007**, *107*, 1272–1295.

(23) Riboli, F.; Caselli, N.; Vignolini, S.; Intonti, F.; Vynck, K.; Barthelemy, P.; Gerardino, A.; Balet, L.; Li, L. H.; Fiore, A.; Gurioli, M.; Wiersma, D. S. Engineering of light confinement in strongly scattering disordered media. *Nat. Mater.* **2014**, *13*, 720–725.

(24) Conley, G. M.; Burresi, M.; Pratesi, F.; Vynck, K.; Wiersma, D. S. Light Transport and Localization in Two-Dimensional Correlated Disorder. *Phys. Rev. Lett.* **2014**, *112*, 143901.

(25) García, P. D.; Stobbe, S.; Söllner, I.; Lodahl, P. Nonuniversal Intensity Correlations in a Two-Dimensional Anderson-Localizing Random Medium. *Phys. Rev. Lett.* **2012**, *109*, 253902.

(26) Cao, H.; Ling, Y.; Xu, J. Y.; Cao, C. Q.; Kumar, P. Photon Statistics of Random Lasers with Resonant Feedback. *Phys. Rev. Lett.* **2001**, *86*, 4524–4527.

(27) van Soest, G.; Poelwijk, F. J.; Lagendijk, A. Speckle experiments in random lasers. *Phys. Rev. E: Stat. Phys., Plasmas, Fluids, Relat. Interdiscip. Top.* **2002**, *65*, 046603.

(28) Soukoulis, C. M., Ed. *Photonic Crystals and Light Localization in the 21st Century*; Kluwer: Dordrecht, 2001; p 194.

(29) Riechel, S.; Kallinger, C.; Lemmer, U.; Feldmann, J.; Gombert, A.; Wittwer, V.; Scherf, U. A nearly diffraction limited surface emitting conjugated polymer laser utilizing a two-dimensional photonic band structure. *Appl. Phys. Lett.* **2000**, *77*, 2310–2312.

(30) Cuerda, J.; Rüting, F.; García-Vidal, F. J.; Bravo-Abad, J. Theory of lasing action in plasmonic crystals. *Phys. Rev. B: Condens. Matter Mater. Phys.* **2015**, *91*, 041118.

(31) Novotny, L.; Hecht, B. *Principles of Nano-Optics*; Cambridge University Press, 2007.

(32) Dainty, J. C. The statistics of speckle. In *Progress in Optics*; Wolf, E. M., Ed.; North-Holland: Amsterdam, 1976; Chapter XIV.

(33) Liu, C.; van der Wel, R.; Rotenberg, N.; Kuipers, L.; Krauss, T.; di Falco, A.; Fratalocchi, A. Triggering extreme events at the nanoscale in photonic seas. *Nat. Phys.* **2015**, *11*, 358–363.

(34) Genack, A. Fluctuations, Correlation and Average Transport of Electromagnetic Radiation in Random Media. In *Scattering and Localization of Waves in Random Media*; Sheng, P., Ed.; World Scientific: Singapore, 1990.

(35) Greffet, J. J.; Carminati, R. Relationship between the near-field speckle pattern and the statistical properties of a surface. *Ultramicroscopy* **1995**, *61*, 43–50.